



Multi-wavelength observations and surveys of galaxy clusters

Joana S. Santos

INAF–Osservatorio Astrofisico di Arcetri, Largo Enrico Fermi 5, 50125 Florence, Italy
e-mail: jsantos@arcetri.inaf.it

Abstract. In this contribution we review the basic properties of galaxy clusters in the context of their formation and evolution. We focus on the baryonic components, i.e., the intracluster medium (ICM) and the galaxies, their observables and how these are linked to important physical properties such as the cluster mass. We evaluate evolutionary trends in the ICM and in the cluster galaxy populations by reviewing the latest results on the most distant clusters known so far up to redshift 2. Lastly, we provide an overview of current and upcoming extragalactic surveys that will enable a leap forward in cluster science in the next decade and beyond.

Key words. Galaxy clusters: observations: multi-wavelength; Galaxy evolution; Intracluster medium

1. Introduction

Galaxy clusters are the largest gravitationally bound structures in the Universe, dominated by dark matter (85% of the cluster mass is in the form of a yet unknown particle that interacts only through gravity) but with a significant baryonic content that makes clusters essential astrophysical laboratories and cosmological probes (e.g., Rosati et al. 2002; Voit 2005).

Baryons (or ordinary matter) account for $\sim 15\%$ of the total cluster mass and are divided in two components: 1) the intracluster medium (ICM), comprising 85% of the total baryons, is a hot, optically thin gas that emits X-ray radiation and, 2) galaxies: each cluster contains tens to hundreds of galaxies seen in the radio, UV, optical, far-infrared and X-rays. These are the cold baryons and amount to 15% of the baryonic cluster mass. Galaxies trace the dark matter distribution, an important property that simplifies the overall study of clusters. While the

measurement of the amount of dark matter in a cluster is done indirectly, e.g. via weak lensing (e.g. Umetsu 2010), the baryons, i.e., the ICM and the galaxies, are directly detected in X-rays and in the radio through X-rays, respectively.

2. The formation of galaxy clusters

In the hierarchical scenario of structure formation (Bardeen et al. 1986; Peebles 1993; Coles & Lucchin 1995; Peacock 1999), clusters of galaxies form via the gravitational collapse of rare high density peaks of the initial density fluctuations, with a typical comoving scale of about $10h^{-1}$ Mpc. The statistics on these large virialized objects can be described by a simple analytical formalism developed by Press & Schechter (1974).

The overall dynamics of clusters is dominated by dark matter, which is subject only to gravity. Therefore, considering a purely gravitational scenario and assuming that gas follows

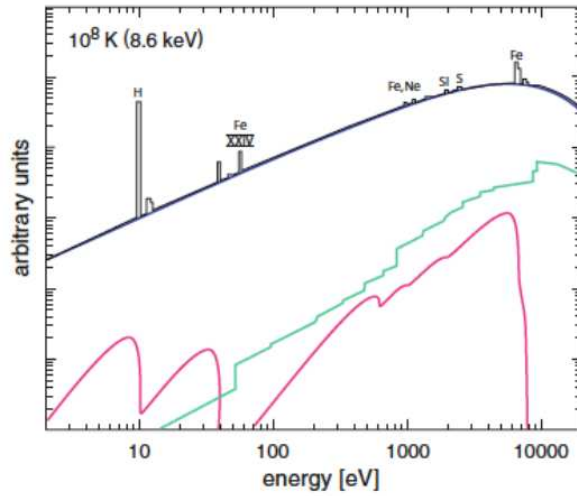


Fig. 1. From Böhringer & Werner (2010). X-ray spectra for solar abundance at 8.6 keV plasma temperatures. The different contributions to the continuum are: Bremsstrahlung (blue), recombination radiation (green), and 2-photon radiation (pink).

the dark matter collapse, clusters are expected to form a regular population, hence a **self-similar** model emerged to characterize clusters in a simple and convenient way: large systems are made of smaller identical systems (Kaiser 1986).

In the **spherical collapse** approximation, a cluster has a well defined boundary corresponding to $\Delta = 18\pi^2 \sim 200$, where Δ is defined as the average density contrast with respect to the critical density of the Universe at the cluster redshift, $\rho_c \equiv 3H^2(z)/8\pi G$ (the critical density is the value required to have a flat Universe). Although clusters are not closed spheres, to a good approximation we can define a cluster as the mass enclosed in a radius corresponding to a fixed Δ , with respect to ρ_c :

$$M_\Delta = \frac{4\pi}{3} r_\Delta \rho_c \Delta_c \quad (1)$$

Self-similarity in the cluster properties allows us to deduce all other cluster properties from the observation of a single global cluster parameter (e.g. X-ray luminosity). However, it is important to note that non-linear processes of collapse and dissipative physical processes cause deviations from self-similarity.

3. Properties of the ICM

In their formation process, galaxy clusters undergo adiabatic compression and shocks providing the primordial heat to the intracluster medium, a hot gas confined by the clusters gravitational potential well. Clusters are permeated by this low-density plasma, which strongly emits X-ray radiation (see Böhringer & Werner 2010 for a recent review) via the following mechanisms:

- free-free: thermal Bremsstrahlung;
- free-bound: recombination;
- bound-bound: deexcitation radiation.

The first two mechanisms are continuum processes and the latter manifests as line emission in the X-ray spectrum. As depicted in Fig. 1 the main emission processes are thermal Bremsstrahlung radiation and metal emission lines, proportional to the square of the gas density. The Bremsstrahlung emissivity ϵ of a plasma at temperature T is given by:

$$\epsilon_\nu \equiv \frac{dL}{dV d\nu} = \frac{2^4 e^6}{3m_3 \hbar c^2} \left(\frac{2\pi k_B T}{m_e c^2} \right)^{1/2} \mu_e n_e^2 g(Z, T, \nu) e^{\frac{h\nu}{k_B T}} (k_B T)^{-1} \quad (2)$$

where ν is the frequency, Z and e are, respectively, the iron and electron charges, m_e is the electron mass, n_e is the electron number density, μ is the mean molecular weight, h_P and k_B are the Planck and Boltzmann constants, respectively, and $g(Z, T, \nu)$ is the Gaunt factor. Integrating ϵ over the X-ray emission energy range and gas distribution, we obtain $L_X \sim 10^{43} - 10^{45} \text{ erg s}^{-1}$.

The ICM is an optically thin plasma (does not require radiative transfer analysis), with a temperature T in the range 2-10 keV, and a density ρ ranging from 10^{-5} cm^{-3} in the cluster outskirts, to 10^{-1} cm^{-3} in the core (note that the mean cosmic density of baryons is $\sim 10^{-8} \text{ cm}^{-3}$).

The ICM is chemically enriched mostly by supernovae (SN) type Ia, with a typical iron abundance of a third of the solar value. Popular plasma radiation codes are the MEKAL (Mewe et al. 1985) and the APEC (Smith et al. 2005) codes, implemented in XSPEC, an X-Ray Spectral Fitting Package (Arnaud et al. 1996).¹

The shape of the X-ray ICM spectrum is a function of the temperature and chemical composition of the plasma, and its normalization is proportional to the plasma density. The element abundances are derived from the intensity of the spectral lines, whereas the temperature is derived from the continuum (Bremsstrahlung). The observed radiation is the result of an integral of radiative emission along the line of sight therefore we need to deproject the spectrum to obtain the deprojected temperature, gas density and metallicity profiles. However, this process is complex and not always feasible, as it requires very good photon statistics and angular resolution.

The main assumption is 3D spherical symmetry, that allows us to fit spectra extracted from a series of concentric annuli simultaneously to account for projection effect. When deprojection is not possible, we have to rely on projected temperature profiles.

3.1. Chemical enrichment

The deep gravitational potential wells of clusters lock metals produced by member galaxies hence the ICM is a fossil record of the chemical enrichment of the cluster environment. Observations have shown that the ICM of local clusters has an average metallicity of $0.3 Z_\odot$ (De Grandi & Molendi 2001; De Grandi et al. 2004). The most common elements found in the ICM are Fe-group elements from SN Ia, and α -elements (O, Ne, Mg) from core collapse supernova (SN II). The most prominent signature of metal enrichment is the Fe K-line complex at 6.7 keV (the only accessible line at high- z). Most of the metals are produced by the bulk of the elliptical galaxies. The main agents of metal ejection are star formation, particularly in the brightest cluster galaxy (BCG), and primordial enrichment of the interstellar medium (ISM) before cluster virialization.

3.2. ICM properties

To determine global cluster parameters, we need to define a fiducial radius. The characteristic or virial radius r_v of a cluster, defined from the theory of structure collapse in an expanding Universe is the radius at which the mean density of the cluster is, $\Delta = 200 \times \rho_c = 3H^2/8\pi G$. Therefore the virial radius of a cluster typically is $r_{200} \sim 1 \text{ Mpc}$. Below we define and describe the ICM properties (Fig. 2).

3.2.1. Surface brightness

Under the physically motivated hypotheses of hydrostatic equilibrium and spherical symmetry, we can describe the X-ray surface brightness with the isothermal β model by Cavaliere & Fusco-Femiano (1976):

$$S(r) \propto (1 + (r/r_c)^2)^{-3\beta+0.5}, \quad (3)$$

where r_c and β are the core radius and slope, respectively. This model is a good description of the observed profiles (Fig. 2 top left panel), with a typical value for β of 2/3. Density radial

¹ <http://heasarc.nasa.gov/xanadu/xspec>

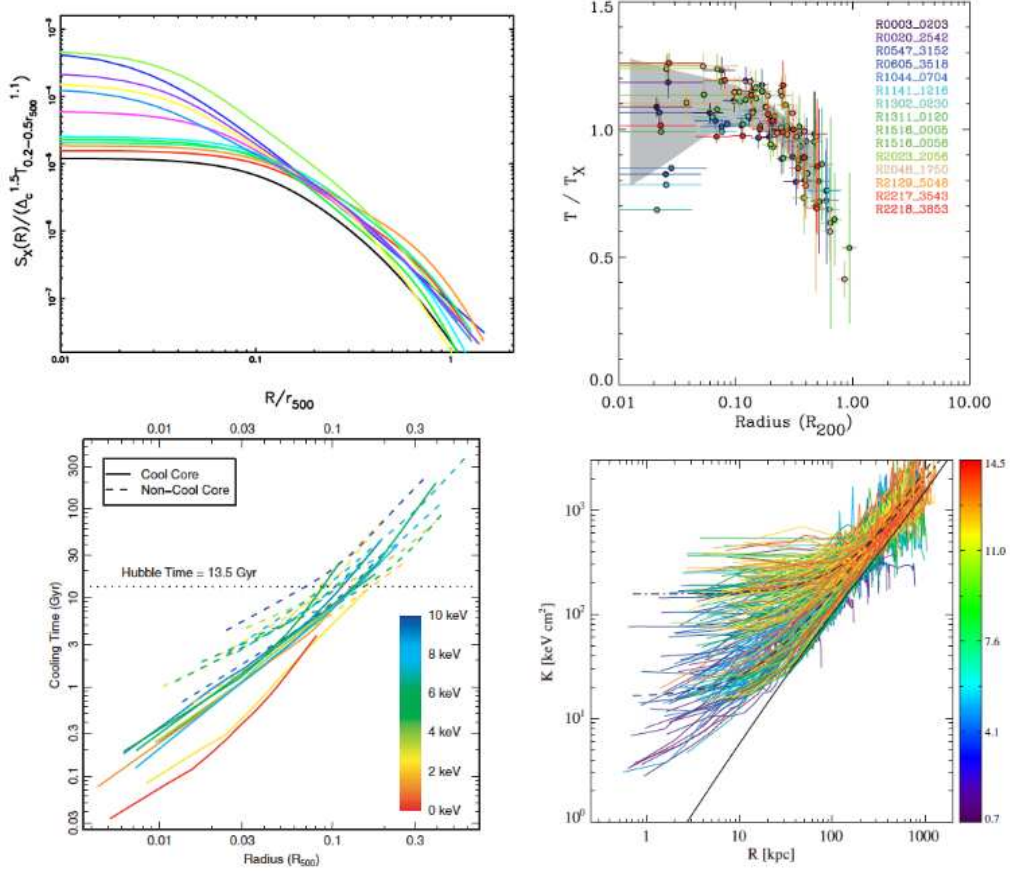


Fig. 2. Radial profiles of ICM properties in local clusters: Surface brightness S_X (top - left), temperature T (top - right), cooling time t_{cool} (bottom - left), entropy K (bottom - right).

profiles are obtained by deprojection of the surface brightness profiles along the line-of-sight:

$$S_X(R) = \int_R^\infty n_e^2 dl \quad (4)$$

where n_e is the electron density and R is the enclosed radius.

3.2.2. Cooling time

The cooling time, t_{cool} , defined as the gas enthalpy per energy lost per volume, $t_{cool} \equiv (d \ln T_{gas} / dt)^{-1}$, provides a time-frame for the evolutionary state of the intracluster

medium. Adopting an isobaric cooling model for the central gas, t_{cool} can be computed as:

$$t_{cool} = \frac{2.5 n_g T}{n_e^2 \Lambda(T)}, \quad (5)$$

where $\Lambda(T)$, n_g , n_e and T are the cooling function, number density of ions and electrons, electron number density and temperature, respectively (Peterson & Fabian 2006).

3.2.3. Entropy

The observed gas entropy results from shock heating of the gas during cluster formation and scales with the cluster temperature (Tozzi &

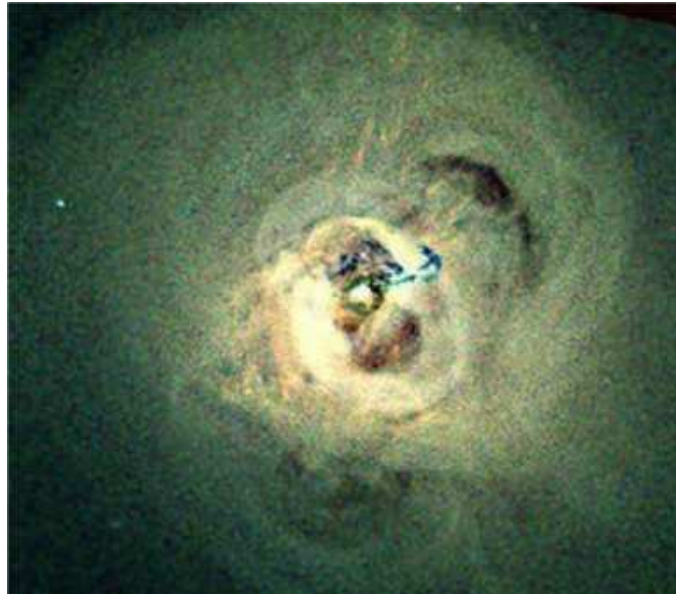


Fig. 3. The Perseus cluster seen in X-rays (from Fabian et al. 2011).

Norman 2001). The thermodynamic history of the ICM is strongly tied to the entropy:

$$K \equiv k_B T n_e^{-2/3}, \quad (6)$$

since K increases with heating and decreases when radiative cooling is dominant, thus preserving a record of the cooling and heating processes in the ICM. However, additional sources of entropy in the ICM are required to explain the observed entropy floor $\Delta K \sim 100 \text{ keV cm}^2$ in local clusters (see Fig. 2 bottom right panel). This excess of entropy with respect to the prediction from pure gravitational collapse can be caused by internal processes related to the BCG feedback (e.g. McNamara & Nulsen 2007; Fabian et al. 2011), or by preheating, a process by which there is early energy injection of entropy in the intergalactic medium before the formation of the cluster through star burst episodes (Tozzi & Norman 2001; Borgani et al. 2005).

3.3. Cool core clusters

In the current model of cluster formation and evolution described above, clusters are expected to cool down radiatively, leading to

what was termed a cooling flow (Fabian et al. 1994), a sink of cold gas (below 1–2 keV) of the order of hundreds to thousands of solar masses per year, that would be detected by strong emission lines in X-ray spectra. However, as X-ray instrumentation capable of detecting such cold gas became available (e.g., the XMM-Newton and Chandra X-ray observatories), observations showed no hint of such cold gas in cluster cores. In fact, the ICM temperature in the observed local clusters is rarely below a third of the global ICM temperature. This indicates that some heating mechanism(s) counteracts the cooling process avoiding the expected catastrophic cooling. Observational and simulation work in the last decade have developed a scenario for the removal of radiatively cooled gas driven by a central radio source (an Active Galactic Nucleus, AGN). Nevertheless, the details on the exact regulation and timescales of the AGN feedback remain unclear (e.g., Peterson & Fabian 2006; McNamara & Nulsen 2007). Currently, the most detailed observation of the intricate feedback process in the core of a cluster is the 1 Msec *Chandra* data of the Perseus cluster, the brightest cluster in the sky in the X-ray band

(Fabian et al. 2011, Fig. 3). The cluster contains a central radio source that has carved bubbles of relativistic plasma into the core of the cluster. These are seen as spectacular cavities in the ICM, that push away the X-ray emitting gas.

The abundance of cool cores on the local cluster population has been extensively studied since the late nineties (Peres et al. 1998). X-ray observations have established that cool cores dominate the local clusters, with a fraction of 50 to 70%, depending on the adopted definition of cool core (e.g. Chen et al. 2007, Dunn & Fabian 2008, Hudson et al. 2010). The main signatures of cool core clusters are:

- central surface brightness peak: can be evaluated with the phenomenological parameter $c_{SB} = SB(r < 40 \text{ kpc}) / SB(r < 400 \text{ kpc})$ (Santos et al. 2008);
- central temperature drop: $T_{core} = 1/3 T_{global}$;
- central entropy threshold: $K_{0,core} = 30 \text{ keV cm}^2$ (Cavagnolo et al. 2009);
- central iron abundance: $Z_{Fe,core}$ may reach the solar value and beyond (De Grandi et al. 2004);
- short central cooling time: $t_{cool,core} < 1 \text{ Gyr}$.

3.4. Merging clusters

Non cool cores make up about half of the local clusters. Most of these show a disturbed ICM morphology indicative of mergers. Cluster mergers are the most energetic events in the Universe after the Big Bang in which subclusters collide at velocities of $\sim 2000 \text{ km/s}$, releasing gravitational binding energy of $> 10^{64}$ ergs (Ferretti et al. 2012). Shocks heat and compress ICM. The main observational evidence that mergers disrupt (partially) cool cores is the presence of substructures, high cooling rates, and high entropy (e.g. Markevitch et al. 1999). Simulations indicate that the preferred channels to disrupt a cool core is through ICM heating caused by merger shocks and ram pressure of the merging sub cluster. The well known Bullet cluster is the best example that illustrates a cluster merger (see Fig. 4 for the thermodynamic maps of this cluster from Million & Allen 2009).

The main thermal effects of mergers are the formation of substructures, cold fronts and merger shocks. Cold fronts are sharp surface brightness discontinuities in merging clusters. Unlike merger shocks there is no pressure jump and the gas temperature in cold fronts is cold. In the case of a merger shock, the velocity shock across the jump, measured from the temperatures on either side of the shock can be computed with the formula (Markevitch et al. 1999):

$$\Delta v_s = v_1 - v_2 = \left[\frac{kT_1}{\mu m_p} (C - 1) \left(\frac{T_2}{T_1} - \frac{1}{C} \right) \right] \quad (7)$$

where C is the shock compression.

Mergers often have non thermal effects:

- large scale diffuse radio sources not connected with individual galaxies produced by high energy relativistic electrons. If located in the cluster center it is termed a radio halo; if located in the outskirts it is termed a radio relic
- soft X-ray emission: Inverse Compton scattering of CMB photons by low energy relativistic electrons
- hard X-ray tails ($> 20 \text{ keV}$): Inverse Compton scattering of CMB photons by high energy relativistic electrons
- high energy cosmic rays.

3.5. Scaling relations

The mass of a cluster is a key parameter to enable the use of clusters as cosmological probes. Because it is not always possible to measure accurate cluster masses (using e.g., temperature and density profiles under the assumption of hydrostatic equilibrium), particularly when conducting large statistical studies with hundreds of clusters, we have to resort to a simpler, general computation of the cluster mass. This can be accomplished by correlating ICM observables and mass via power laws, since clusters are, to a large extent, a self similar family of objects. However, clusters are not only governed by gravitational processes and deviations from self similarity need to be taken into account. This is quantified by the measurement

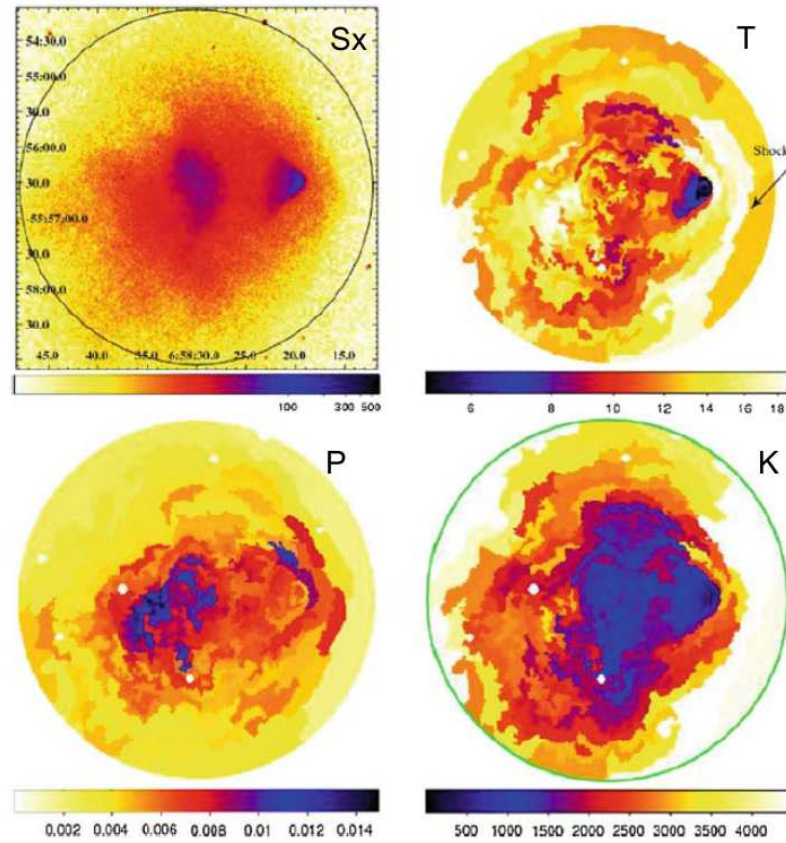


Fig. 4. Thermodynamical maps of the Bullet cluster from Million & Allen (2009). On the top panels are shown the X-ray surface brightness S_X (left), and temperature map T (right), on the bottom panels the pressure P (left) and entropy K (right).

of the scatter in the scaling relations, that informs us of the presence of complex non gravitational activity. Often it is necessary to excise the core from the X-ray analysis, since cluster cores are the seat of feedback processes that do not follow the simple self similar model. A recent compilation of scaling relations is presented in Giodini et al. (2013).

4. Properties of galaxies in clusters

4.1. Morphology

Galaxies in clusters are broadly divided in early- and late-type galaxies. Early-types are bulge dominated, typically ellipticals and S0s. They are massive (up to few $10^{12} M_\odot$), show

red colors, and are passively evolving, i.e., star formation is quenched. The main spectral features are the Balmer/4000Å break and Mg absorption lines. In contrast, late-type galaxies have a disk structure, bluer colors that indicate on-going star formation, and their spectral features include emission lines, e.g., H α .

To evaluate galaxy morphology we may perform a visual classification based on calibrated templates, or take a model approach. The most commonly used description of a galaxy's surface brightness profile is the Sersic model (Sersic 1968),

$$\Sigma(r) \propto \exp(-((r/r_e)^{1/n} - 1)), \quad (8)$$

where Σ is the surface brightness at radius r , n indicates the concentration of the profile

and r_e encloses half of the galaxy light. For $n=4$ we have the widely used De Vaucouleurs model. We can then perform a morphological study based on the structural parameters n and r_e (with the caveat that there is a degeneracy between these parameters). Studies have shown that ellipticals have high index $n (>2)$ and disk galaxies have low index $n (<2)$ and require an additional model component (exponential disk) for a proper description of the surface brightness profile (e.g. Fisher & Drory 2008).

A fundamental relation based on the study of galaxies in clusters and their evolution emerged a few decades ago, the **morphology-density** relation (Dressler 1980), which states that the fraction of galaxies of different morphological types in a region depends on the overall density of the environment. Observations showed that the fraction of spiral galaxies falls for increasing local density, compensated by a rise in the fraction of elliptical and S0s, thus the cores of clusters are dominated by early type galaxies.

4.2. Colour-magnitude relation

Galaxy clusters are characterized by an old population of passively evolving galaxies, forming a distinct and tight sequence of galaxies in the color-magnitude relation, the red-sequence (RS, Baum 1959; Visvanathan & Sandage 1977). In addition to the RS, a more broadly distributed population of blue late-type galaxies is also present in the CMR of galaxy clusters, evidencing a color bimodality strongly dependent on the stellar content of galaxies (Strateva et al. 2001). The CMR is described by the following parameters: the *zero point* that is related with the age of cluster; the *scatter* of the RS that accounts for galaxy age variations; and the *slope* that is related with the galaxies metal content.

We note that the locus of the red-sequence is a rough photometric redshift since it requires only 2 bands to get an estimate of the cluster RS and consequently the cluster redshift. Therefore, as will be discussed later on, the CMR and the study of the red-sequence is a

powerful method to detect clusters and obtain an approximate cluster redshift.

4.3. Synthetic stellar populations

The use of models based on stellar evolution theory is a standard technique to study the stellar content in galaxies, to constrain stellar masses, ages and star formation histories. Most models assume a Simple Stellar Population (SSP) where a single burst of star formation took place, with equal metallicity. However, it is more realistic to consider that the star formation history of galaxies (SFH) is due to a series of instantaneous bursts, therefore stellar populations are better described with composite stellar populations. An important component in synthetic stellar population studies is the choice of an initial mass function (IMF), describing the relative frequency with which stars of various masses are formed. IMFs will be discussed in the next subsection.

The study of local galaxies using this technique has allowed us to understand crucial characteristics of the star formation histories (SFHs) of galaxies. First of all, it has been shown that the environment impacts galaxy evolution: Thomas et al. (2005) showed that field galaxies (low density environments) are 1–2 Gyr younger than their counterparts in clusters (high density environment). In addition, SFHs are mass dependent: the more massive elliptical galaxies have SFHs peaking at higher redshifts ($z \geq 3$ in clusters) than less massive galaxies. This result is in apparent conflict with expectations based on the hierarchical growth of DM haloes. However, if we allow a late mass assembly via dry mergers where small gas-free galaxies merge to form larger galaxies, then stars in massive galaxies are old even if the galaxies formed recently.

4.4. Star formation

Young stellar populations in galaxies emit the bulk of their energy in the rest-frame UV. The main star formation indicators are:

- ultraviolet flux;
- optical emission lines: $H\alpha$, [OII];

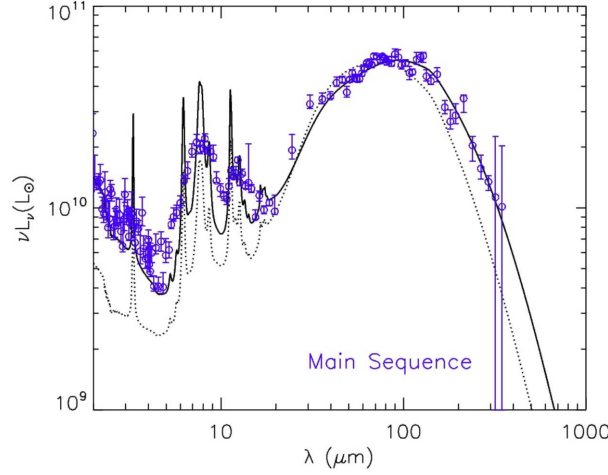


Fig. 5. Typical SED of main-sequence and starburst galaxies from Elbaz et al. (2010).

– far infrared emission: dust absorbs UV very efficiently and reradiates in the FIR.

A couple of caveats are important to mention: the first two diagnostics are sensitive to dust therefore there has to be an independent assessment of dust via SED fitting or via the Balmer decrement ($H\alpha/H\beta$). In addition, the [OII] line emission suffers contamination by AGN activity (see the reviews Calzetti 2013; Kennicutt & Evans 2012).

In order to use these diagnostics we need to convert luminosities to star formation rates. This is accomplished with a set of calibrations, that are empirical/model-based relations used to convert luminosity to SFRs. This conversion assumes the SFR has been roughly constant over the timescale probed by the specific emission used and the stellar IMF is known and fully sampled. Recently, the review by Kennicutt & Evans (2012) collected an updated set of calibrations of the form:

$$\log \dot{M}_*(M_\odot/\text{yr}) = \log L_x - \log C_x \quad (9)$$

where L_x is the luminosity and C_x is the logarithmic SFR calibration constant. These calibrations are based on evolutionary synthesis models, in which the SEDs are derived from synthetic stellar populations with a prescribed age mix, chemical composition, and IMF. The three most often used IMFs are:

- $\chi(M) \propto M^{-0.3}$, $M/M_\odot < 0.08$
- $\chi(M) \propto M^{-1.3}$, $0.08 < M/M_\odot < 0.5$
- $\chi(M) \propto M^{-2.3}$, $0.5 < M/M_\odot$
(Kroupa 2001);
- $\chi(M) \propto e^{-(\log m - \log m_c)2/2\sigma^2}$, $M/M_\odot < 1$
- $\chi(M) \propto M^{-1.3}$, $M/M_\odot > 1$
(Chabrier 2003);
- $\chi(M) \propto M^{-2.35}$, $0.1 < M/M_\odot < 100$
(Salpeter 1955).

Because most of the star formation at $z \sim 1$ is enshrouded in dust, the far infrared is a powerful diagnostic for star formation as it provides a direct measure of the reprocessed UV light from the on-going star formation. The *Herschel* Space Observatory (Pillbrat et al. 2010) that operated between 2009-2012 in the 70-500 μm regime enabled a step forward in the study of the cold Universe, and despite its limitations (an angular resolution of 35'' which implies reaching confusion noise at the longest wavelengths), provided new insights on the SF properties at high redshift. In particular, an empirical relation between stellar mass and SFR (e.g. Daddi et al. 2007; Elbaz et al. 2011) is now established, described by $\text{SFR} \propto M_*^\alpha$ present out to $z \sim 3$, populated by a so-called main sequence (MS) of galaxies (see Fig. 5), and a group of galaxies that are offset from this MS that have significantly higher SFRs - the starbursts (Fig. 6). The MS relation implies two

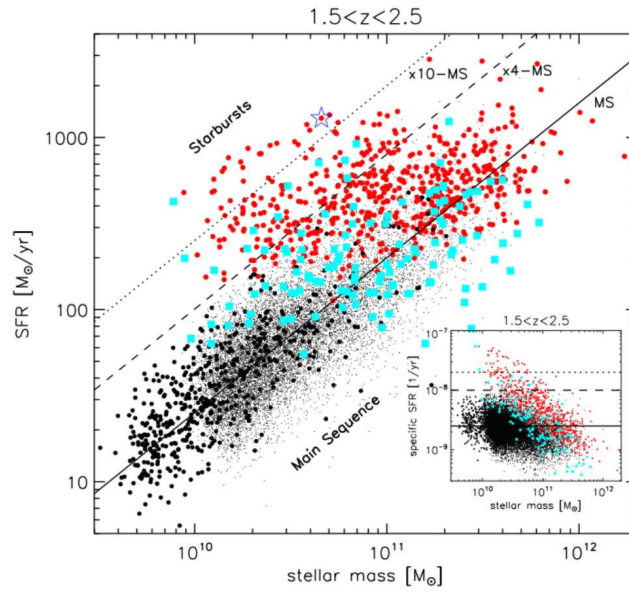


Fig. 6. The SFR- M_* for galaxies at high redshift from Rodighiero et al. (2011), showing the main-sequence (black and cyan symbols) and the starburst (red) galaxies.

modes of star formation: 1) the gradual formation of stars in gaseous disks (main sequence galaxies), and 2) the high-intensity epochs of star formation known as starbursts, expected to result from major galaxy mergers (Daddi et al. 2010; Genzel et al. 2010).

4.5. Environmental processes in clusters

Several physical processes take place in the biased environments of galaxy clusters that affect the galaxy properties described above (e.g., Treu et al. 2003). These processes are divided in three categories:

- galaxy interactions with the cluster potential well: tidal compression of galactic gas by interaction with the cluster potential can increase the star formation rate; tidal stripping of the outer galactic regions by the cluster potential;
- galaxy-galaxy interactions: mergers (low speed interactions between galaxies of similar mass); harassment (high speed interactions between galaxies);
- galaxy interactions with the ICM: ram-pressure stripping (removal of galactic gas

by pressure exerted by the intracluster medium, see Fig. 7).

4.6. The brightest cluster galaxy

The central regions of massive galaxy clusters typically host a very bright and massive ($10^{12} M_*$) galaxy, the brightest cluster galaxy (BCG), usually an early-type galaxy (elliptical, S0). Simulation work (e.g., De Lucia & Blaizot 2007) points to a scenario in which BCGs develop through the accretion of a small number of objects with $M_* > 10^{10} M_\odot$, with very low gas fractions and SFRs, the so-called dry mergers. Therefore, although the bulk of the stars in BCGs forms early ($z > 3-5$), the final BCGs assemble from small progenitors rather late, by $z \sim 0.5$.

The properties of BCGs are governed by their large stellar content and ubiquitous location at the bottom of the potential well of their host cluster (von den Linden et al. 2007). In relaxed clusters, BCGs are coincident with the peaks of X-ray emission and are connected with the presence of a cool core, with observations showing that BCGs are the main con-



Fig. 7. MUSE/VLT view of the ram-pressure stripped galaxy ESO 137-001 (image credit ESO, <http://www.eso.org/public/news/eso1437/>)

tributor to the Fe content in the ICM core (De Grandi et al. 2014).

5. High-redshift clusters: evolutionary trends

In the last decade there has been a significant advancement in observational efforts to detect and characterize clusters at $z > 1$. This is a challenge though because the small size (angular size, $D_A = (1+z)/D_L$, where D_L is the luminosity distance) and faintness (surface brightness dimming, $\propto (1+z)^{-4}$) of distant clusters require telescopes with large apertures and photon collecting power. However, statistical studies of $z > 1$ clusters are crucial to understand the formation of galaxy clusters and their connection to proto-clusters (unvirialized galaxy systems that will collapse into a cluster). In this section we discuss the evolutionary trends in the ICM and in the galaxy populations of clusters that have emerged in the last decade.

5.1. Evolutionary trends in the ICM

Using a sample of 56 clusters at $0.2 < z < 1.2$, Balestra et al. (2007) studied the evolution of the iron abundance in the ICM. Their results showed that the ICM is already significantly enriched at a lookback time of 9 Gyr, $Z_{Fe} \sim 0.25 Z_{\odot}$, which suggests a mild evolution of the iron content in the ICM: $\langle Fe \text{ (ICM)} \rangle$ today is $\sim 1.5\times$ larger than at $z \sim 1.2$ (Fig. 8).

The evolution of cool cores up to redshift 0.4 was reported in Bauer et al. (2005) that showed that the fraction of cool cores does not significantly evolve up to $z \sim 0.4$, since clusters in this redshift range have the same temperature decrement (about one-third), as the nearby CC's, and their central cooling times are similar. Studies at $z > 0.5$ become more challenging due to the small size and faintness of the clusters and a simple approach based on the surface brightness core-to-bulk ratio demonstrated to be the most effective diagnostic of cool cores (Santos et al. 2008). Using

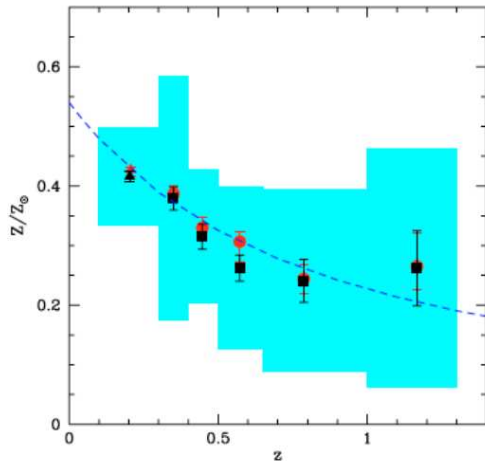


Fig. 8. Evolution of the Fe abundance out to $z=1.3$ from Balestra et al. (2007). The data points are shown in black and red, the errors are depicted by the cyan band and the dashed line ($Z=Z_0(1+z)^{1.25}$) indicates the best fit over the redshift bins.

the phenomenological parameter $c_{SB} = SB(<40 \text{ kpc}) / SB(<400 \text{ kpc})$, Santos et al. (2008, 2010) showed that at $0.7 < z < 1.4$ there is a moderate evolution of the cool core fraction, in which most high- z clusters are moderate CC. The first evidence for the existence of cool core clusters at $z=1$ was presented in Santos et al. (2012), using very deep *Chandra* data of the cluster WARPJ1415.1+3612 ($z=1.03$). This data allowed, for the first time, to measure a temperature and metallicity profile of the ICM of a distant cluster (Fig. 9), showing the standard signatures of a cool core. In particular, the iron abundance in this cluster has an unprecedented value of $3 Z_{\odot}$, which suggests that the chemical enrichment mechanisms in the ICM happen very early in the formation of a cluster.

The recent discovery and study of the Phoenix cluster (SPT-CLJ2344-4243, McDonald et al. 2012), a massive system at $z=0.6$ discovered through the SZ effect, suggested the presence of a cooling flow, i.e., a sink of cold gas below 1 keV. However, this hypothesis has not been confirmed, even with very deep *Chandra* data (McDonald et al. 2015).

5.2. Evolutionary trends in the galaxy populations

5.2.1. The BCG

Massive BCGs are found out to $z \sim 1.4$. Beyond that they appear to be in a phase of assembly, with instances of star formation and AGN activity. Predictions from the standard hierarchical model claim that BCGs should evolve much faster than satellite galaxies (e.g., Shankar et al. 2013). The evolution of the size and mass of BCGs has recently been investigated out to redshift ~ 1 . Results on the size evolution of BCGs are still controversial, ranging between little (Weinmann et al. 2009) to strong size evolution up to $z \sim 1.3$ (Bernardi 2009). In addition, a study by Huertas-Compagny et al. (2013) suggests that BCGs and satellite galaxies of similar stellar mass ($\log(M_*/M_{\odot}) > 11$) evolve in a similar way, which is in disagreement with hierarchical models. Lidman et al. (2012) have recently shown that the stellar mass of BCGs increases by a factor ~ 2 from $z=0.9$ to 0.2 (see Fig.10). Most of the mass build up is thought to occur through dry mergers.

5.2.2. The CMR

Current studies have shown no significant evolution in the CMR parameters out to redshift $z \sim 1.3$ (Mei et al. 2009). Recently though, Gobat et al. (2011) presented a study of a group/cluster at $z=2$ where the red-sequence is no longer the distinct and tight population as seen in local clusters. Even though this is just one system, this epoch may mark the beginning of the formation of the red-sequence. However, a statistical study needs to be conducted in the redshift range 1.3–2.0 before reaching a general conclusion.

5.2.3. The Morphology-density relation

While at low redshift the fractions of all morphological types appear to be independent of the cluster mass, at redshift >0.9 results have shown a stronger evolution of the spiral and S0 fractions in less massive clusters and an un-

changed fraction of ellipticals (Poggianti et al. 2009).

5.2.4. Star formation histories

The SFHs of local ETGs in the field are found to be 1 – 2 Gyr younger than their counterparts in clusters. At $z \sim 1$, a study by Gobat et al. (2008) compared the SFHs of ETGs in the cluster RDCS J1252.9-2927 at $z=1.2$ vs GOODS field galaxies at the same redshift. They find that cluster galaxies form the bulk of their stars ~ 0.5 Gyr earlier than their counterparts in the field, with massive ETGs having already finished forming stars at $z > 1.5$ in both environments. This result indicates that at higher redshift ($z \gtrsim 1$) the differences between the SFHs of ETGs in clusters and in the field are smaller than in the local Universe.

5.2.5. Star formation rate

In the local Universe it has been observed that star forming galaxies prefer low galaxy density environments, i.e., the field relative to clusters, and the cluster outskirts relative to the core. However, because the cosmic SFR peaks at $z \sim 1$ (Madau et al. 1996) we expect to see star forming galaxies even in the most dense environments - that of cluster cores - at $z \gtrsim 1$.

Elbaz et al. (2007) showed the reversal of this **star formation–density** relation in a sample of field galaxies at $z \sim 1$. At higher redshift, Tran et al. (2010) confirmed the same trend in a galaxy group at $z=1.6$, and more recently, the reversal of the SF–density relation was shown in a massive cluster at $z=1.6$ (Santos et al. 2015).

On the other hand, the evolution of the SFR– M_* relation with redshift appears to remain unchanged with the exception of the zero point, that increases with redshift. This is interpreted as the amount of gas in galaxies that drives the path of a galaxy in the MS plane.

The mass-normalized cluster SFR, obtained by dividing the total SFR by the cluster mass, SFR/M_g , has been widely used to quantify the evolution of the global SFR in clusters with redshift. Recently, Webb et al. (2013)

used a representative sample with 42 clusters selected in the infrared and derived SFRs from 24 μm fluxes to parametrize the redshift evolution of the SFR/M_g up to $z \sim 1$. The authors fit a power law to the data $\propto (1+z)^{5.4}$, indicating a rapid increase of the mass-normalized SFR with redshift. Similarly, (Popesso et al. 2015) present empirical relations for the evolution of the SFR/M_g for groups and clusters based on *Herschel* data,

$$\Sigma(SFR)/M = (60 \pm 18) \times z^{0.7 \pm 0.2}. \quad (10)$$

The recent result of Santos et al. (2015) on the FIR study of the massive cluster XDCP J0044.0-2033 at $z=1.58$ indicates a SFR/M_g a factor 12 \times higher than the empirical expectations of Popesso et al. (2015) (Fig. 11). The main caveat for these empirical predictions is the limited redshift range of the samples used, $z < 1$, and small sample statistics.

5.3. Gallery of distant clusters

In this section we describe some of the most distant, well studied clusters known to date.

5.3.1. XMMUJ 2235.3 - 2033 at $z=1.39$

The cluster XMMUJ 2235.3 - 2033 was discovered as extended X-ray emission in XMM-Newton data by the XMM-Newton Distant Cluster Project (XDCP, Mullis et al. 2005). The ICM properties were analyzed with 200 ksec of *Chandra* in Rosati et al. (2009) that confirmed a very massive system, with $M_{200} = 6 \times 10^{14} M_\odot$. Surprisingly this cluster at $z \sim 1.4$ has a regular morphology, with indication of a cool core. The ICM temperature is quite high, $T = 8.6 \pm 1.2$ keV, and the 6.7 keV Fe line was detected indicating a global metallicity $Z = 0.26_{-0.16}^{0.20} Z_\odot$. The cluster galaxy population was studied using HST and VLT data as described in Strazzullo et al. (2010). This study showed that the galaxies in the core (< 250 kpc) are very old, massive ($10^{11} M_*$), and passive, and are dominated by a prominent BCG, 1 mag brighter than next brightest galaxy. There is a strong mean age radial gradient: core galaxies have $z_f \sim 5$, whereas galaxies in the outskirts have $z_f \sim$

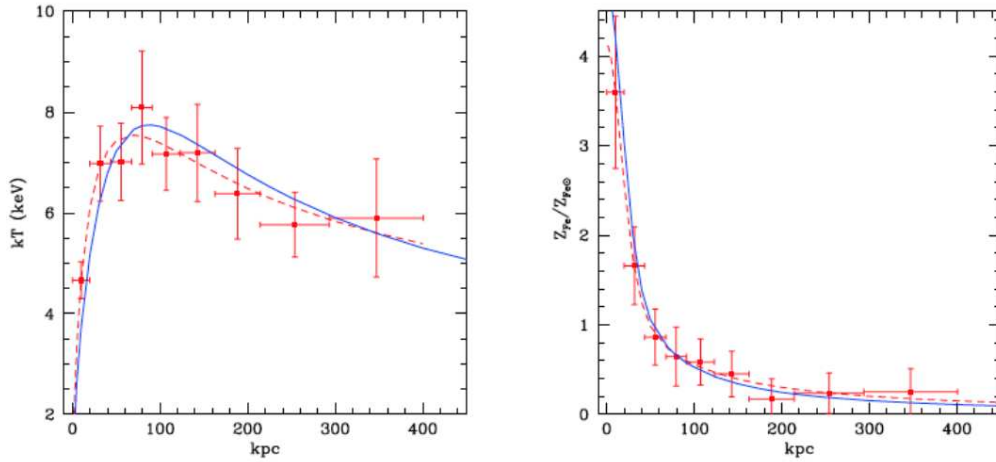


Fig. 9. Temperature (left) and iron abundance (right) radial profiles of WARP J1415 at $z=1.03$ from Santos et al. (2012).

2 and the CMR is firmly in place, displaying a tight red-sequence with early-type morphology.

5.3.2. SPT-CL J 2040-4451 at $z=1.478$

The most distant cluster discovered using the Sunyaev-Zeldovich effect is SPT-CL J 2040-4451 at $z=1.478$ (Bayliss et al. 2014) detected by the South Pole Telescope. This is a very massive cluster with a reported total mass $M_{200,SZ} = 5.8 \pm 1.4 \times 10^{14} M_{\odot}$. The cluster has 15 cluster members confirmed, all of them with [OII] emission, and located beyond the core (250 kpc). The derived individual SFRs are relatively low, $< 25 M_{\odot}/\text{yr}$.

5.3.3. XDCP0044.0-2033 at $z=1.58$

The cluster XDCP0044.0-2033 at $z=1.58$ is the most distant cluster in the XDCP survey (Santos et al. 2011). A very deep *Chandra* observation (380 ksec) enabled the detailed analysis of the ICM revealing a massive cluster with $M_{200} = (4.7^{+1.4}_{-0.9}) \times 10^{14} M_{\odot}$, and a tentative detection of the 6.7 keV Fe line, which would indicate an early chemical enrichment of the ICM (Tozzi et al. 2015). A far infrared study using *Herschel* data (Santos et al. 2015). con-

firmed a reversal of the SF-density relation in the cluster: the SFR in the core is $\geq 1900 M_{\odot}/\text{yr}$, a value very high and much larger than the SFR in the cluster outskirts, $\text{SFR} (500 < r < 1000 \text{ kpc}) \geq 200 M_{\odot}/\text{yr}$. Optical data show evidence for merger activity in core, and a BCG in formation (Fassbender et al. 2014).

5.3.4. CLG0218.3-0510 at $z=1.62$

CLG0218.3-0510 at $z=1.62$ was discovered as an overdensity of red galaxies in *Spitzer* (Papovich et al. 2010) and as weak X-ray emission in XMM-Newton data (Tanaka et al. 2010). This is a low mass cluster or group, with an upper limit on the mass of $5-7 \times 10^{13} M_{\odot}$ (Tanaka et al. 2010). Using infrared data from *Spitzer* – MIPS, Tran et al. (2010) confirmed a reversal of the SF-density relation within $r < 1$ Mpc, in which the total SFR in the cluster, $\sim 1500 M_{\odot}/\text{yr}^{-1}$, is significantly higher than the SFR in a local cluster with similar progenitor mass. The zeropoint and scatter of the CMR for red-sequence galaxies imply a formation epoch of $z_f \sim 2.3$, the time of the last major SF episode in the red galaxies.

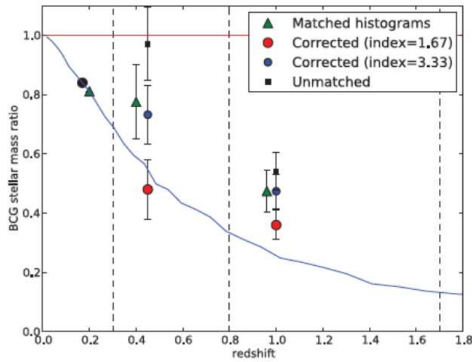


Fig. 10. Evolution of the mass of the BCG up to $z \sim 1$ (from Lidman et al. 2012).

5.3.5. CL J1449+0856 at $z=2.0$

Discovered as an overdensity of infrared galaxies, CL J1449+0856 at $z=2.0$ is the most distant group/cluster known to date (Gobat et al. 2011). This is also one of the first systems studied with HST/WFC3 slit less spectroscopy, that enabled a first direct spectroscopic confirmation of quiescent galaxies in a $z \sim 2$ group/cluster (Gobat et al. 2013). The study of the galaxy population showed that the core is dominated by passive red galaxies, with ~ 1 Gyr, though there are star forming galaxies too. There is no tight red-sequence and the BCG appears to be in a stage of assembly and hosts a central X-ray bright AGN. The measurement of the galaxy sizes showed that passive early types are $2-3\times$ smaller than local counterparts but on average $2\times$ larger than $z \sim 2$ field galaxies.

6. Current and future cluster surveys

6.1. Cluster detection techniques

6.1.1. X-rays

For a review on X-ray cluster detection techniques see Valtchanov et al. (2001). Here we describe two of the most often used techniques:

- 1) Wavelet technique (e.g. Rosati et al. 1995): convolution of an image with a wavelet function

$$w_a(x, y) = I(x, y) \otimes \psi(x/a, y/a) \quad (11)$$

The original image is decomposed into a number of wavelet coefficient images, over a set of scales a (e.g. Gaussian kernel).

- 2) Voronoi-Tessellation & Percolation (Ebeling & Wiedenmann 1993; Liu et al. 2015): general method to detect structures in a distribution of photons by choosing regions with enhanced surface density relative to an underlying Poisson distribution. Each photon defines a centre of a polygon where the surface brightness (SB) is given by the inverse of the area of the polygon. Comparing the distribution function of SB to the one expected from a Poisson distribution, cells above a given threshold are percolated.

6.1.2. Optical / Infrared

- 1) Red-sequence (Gladders & Yee 2000): galaxy clusters exhibit a well-defined red sequence of galaxies. The RS can be defined by choosing a color appropriate for the desired redshift regime. This method is based on the construction of color slices from the data and, followed by the search for overdensities of galaxies in these slices. Once significant overdensities are found, the slice containing the peak signal for the overdensity gives the cluster candidate's most probable redshift.
- 2) Matched Filter (Postman et al. 1996; Milkeraitis et al. 2010): clusters show a typical dark matter density profile and galaxies trace the DM. This method works by selecting regions in the sky where the distribution of galaxies corresponds to the projection of average cluster profile. It is possible to specify additional info (e.g. z , galaxy luminosity function), for more stringent results. The matched subfilters enable the extraction of a signal corresponding to the existence of a cluster.
- 3) $P(z)$ wavelet (Brodwin et al. 2006): this method is based on the construction of redshift probability functions, $P(z)$, for each galaxy and subsequent generation of

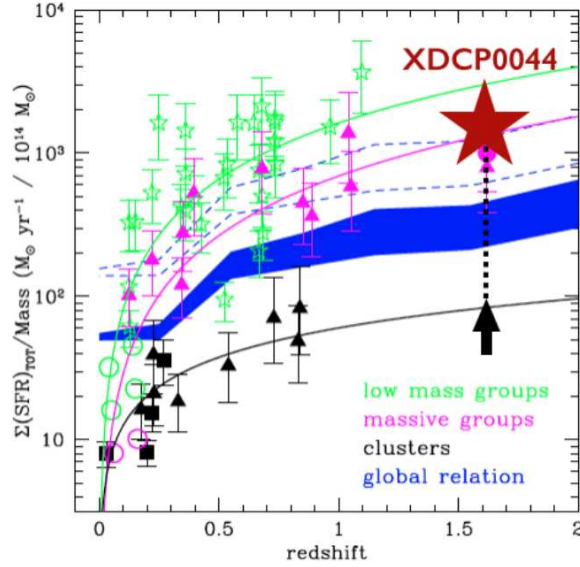


Fig. 11. Evolution of the SFR per halo mass in groups (green, magenta), and clusters (black) from Popesso et al. (2015). The SFR/ M_g of the massive cluster XDCP0044 at $z=1.6$ is indicated by the red star Santos et al. (2015) while the black arrow shows the expected SFR/ M_g value for a massive cluster at that redshift.

probability maps in small redshift slices (e.g. $\delta z = 0.2$). A wavelet analysis is then performed, tuned to detect structures on ~ 500 kpc scales.

- 4) Redmapper (Rykoff et al. 2013): a red-sequence photometric cluster finder that iteratively self trains a model of RS galaxies (calibrated with spectroscopic redshifts), then "grows" a cluster centered about every (z -phot) galaxy. Galaxies are ranked in terms of probability to be the BCG. Once a rich cluster is identified ($\lambda \geq 5$, number RS galaxies hosted by cluster) the algorithm computes the cluster photometric redshift.
- 5) Weak lensing Umetsu (e.g. 2010): the deep gravitational potential wells of clusters of galaxies generate weak shape distortions of the images of background sources due to differential deflection of light rays, resulting in a systematic distortion pattern of background source images around the center of massive clusters.

6.1.3. Sunyaev - Zeldovich effect

The SZ effect is a spectral distortion imposed on the 2.7 K CMB radiation when the microwave photons are scattered by the hot gas in galaxy clusters (Inverse Compton scattering). The Compton parameter y is a measure of the gas pressure integrated along the line-of-sight:

$$y = (\sigma_T/m_e c^2) \int P dl, \quad (12)$$

where σ_T is the Thomson cross-section, and P is the pressure, $P = n_e T$. The total SZ signal, integrated over the cluster extent, is proportional to the integrated Compton parameter Y_{SZ} Arnaud et al. (2010),

$$Y_{SZ} D_A^2 = (\sigma_T/m_e c^2) \int P dV. \quad (13)$$

6.2. Proto-cluster detection techniques

6.2.1. High- z radio galaxies

Distant radio galaxies are among the largest, most luminous and massive objects in the

Universe and are believed to be powered by accretion of matter onto SMBH in the nuclei of their host galaxies (Miley & De Breuck 2008; Venemans et al. 2007). They are embedded in giant ionized gas halos surrounded by galaxy overdensities, covering a few Mpc and the radio galaxy hosts have clumpy optical morphologies, extreme SFR, and large stellar mass. The best example of a proto-cluster detected with this technique is the Spiderweb galaxy at $z=2.2$ (Miley et al. 2006). Statistics are consistent with every dominant cluster galaxy having gone through a luminous radio phase during its evolution.

6.2.2. QSOs at $z > 4$

Quasars (QSOs) at $z > 5$ may also be a tracer of proto-clusters (Bañados et al. 2013). The motivation for this technique is based on the known correlation between the black hole mass with the mass of the dark matter halo in nearby galaxies. The detection of proto-clusters is performed by selecting star-forming galaxies (Ly α emission galaxies) around QSOs. An important caveat to consider is that QSO emission may be a hostile environment and quench star formation.

6.2.3. Planck blobs

The recent advent of the all-sky *Planck* mission that operated in the microwave and radio regime, enabled the development of a new technique to select proto-clusters, based on the analysis of the *Planck* maps (100 μ m – 100 GHz). The method is in essence a color selection, after cleaning the maps from CMB and Galactic dust. The next step is to look for counterparts in the maps of *Herschel*/SPIRE at 250–500 μ m that have a better resolution relative to the *Planck* maps. Red sources (350 μ m peakers / 500 μ m risers) with a FIR counterpart are either bright lensed sources or overdensities of star forming galaxies. To date five blobs have been confirmed at $z > 1.7$ (Dole 2015).

6.3. Clusters as cosmological probes

Galaxy clusters are also tracers of the large-scale structure, making them powerful tools to constrain the cosmological parameters Ω_m , σ_8 and, to a lesser degree, Ω_Λ . Here we summarize the methodologies based on X-ray observations of clusters to constrain cosmological parameters (for a review on this topic see Allen et al. 2011):

- mass function of local clusters, $n(M)$;
- gas mass fraction in clusters, f_{gas} ;
- evolution of the cluster mass function, $n(M,z)$.

The important quantity to measure (regardless of the type of observation) is the cluster mass, therefore we list here the main methodologies to obtain cluster masses:

- Dynamical analysis from galaxy kinematics: cluster velocity dispersion, $M=3 \sigma^2 R/G$;
- Richness: N_{200} , number of red-sequence galaxies within a scaled radius such the $\langle galaxy(<r) \rangle$ is $200 \times \rho_{crit}$. $N_{200} \sim 10-100$ (Rozo et al. 2012);
- Weak & strong lensing: measure of the shapes of background galaxies and compare them with the expectations for an isotropic distribution of galaxies (e.g. Umetsu 2010);
- Sunyaev - Zeldovich effect:

$$y = \int_{k_B T}^{m_e c^2} \sigma_T n_e dl \propto \int n T dl \quad (14)$$

- X-rays: scaling relations (e.g., $L_X - M$);
- X-rays: cluster mass computed under the hypothesis of Hydrostatic Equilibrium (HE) which determines the balance between the pressure and the gravitational forces:

$$M_{HE}(<r) = - \frac{r k_B T(r)}{G \mu m_p} \left[\frac{d \ln \rho_r}{d \ln r} + \frac{d \ln T r}{d \ln r} \right]. \quad (15)$$

6.4. Extragalactic surveys: current and future prospects

In this final section we provide a brief overview of recent and upcoming extragalactic surveys with a focus on cluster science.

6.4.1. Planck

Planck was an ESA mission with NASA involvement that operated in 2009-2012 and performed an all sky survey with the instruments HFI (83 - 857 GHz) and LFI (27 - 77 GHz). The primary science goals of Planck are cosmological: map the CMB anisotropies with improved sensitivity and angular resolution and measure the amplitude of structures in the CMB. However important science has been done on clusters, and continues to be exploited, based on measurements of the Sunyaev-Zel'dovich effect (SZ). The Planck catalogue of SZ sources (arXiv:1303.5089) comprises 861 confirmed clusters, 683 of which were previously-known, 178 are newly confirmed and 366 are candidates. Planck clusters appear to be X-ray under-luminous for their masses and 70% of the new clusters have disturbed morphologies (Planck Collaboration 2015).

6.4.2. South Pole Telescope

The South Pole Telescope (SPT, PI Carlstrom) is a 10 m telescope operating in the millimeter wavelength, optimized for low noise measurements of the CMB. The SPT experiment consists of three completed, underway or planned surveys: 1) SPT-SZ (2007-2011) with 2500 deg², 1000 detectors; 2) SPTpol (2012-2015) 1600 detectors; 3) SPT-3G (2016-2017) 15 000 detectors. The SPT-SZ survey has provided a new catalog of approximately 500 of the most massive, distant clusters in the Universe, about 75% of which are new discoveries (Benson et al. 2013).

6.4.3. Atacama Cosmology Telescope

The Atacama Cosmology Telescope (ACT, PI Jimenez) is a 6 m telescope located in Chile. ACT observes simultaneously in 3 frequency bands centered on 148 GHz, 218 GHz and 277 GHz. A catalog of 68 clusters (19 new discoveries) in the redshift range $0.1 < z < 1.4$ within an area of 504 square degrees was published in Hasselfield et al. (2013).

6.4.4. Dark energy survey

The Dark Energy Survey (DES) is an optical *ugriz* survey using the DECam camera with a FOV of 2.2 deg² mounted on the 4 m Blanco telescope in Chile. DES began in September 2013 and will continue for 5 years. It will map 1/8th of the sky (5000 deg²) in unprecedented detail. The goal of DES is to investigate the nature of Dark Energy (DE) by combining SN Ia, BAO, Galaxy clusters and Weak Lensing. DES is expected to have a major impact in cluster science with an expected number of 100 000 galaxy clusters detected. This will allow for a robust measurement of cosmological parameters using cluster counts (clusters detected via the red sequence technique) and gravitational lensing.

6.4.5. Euclid

Euclid is an ESA led space mission aimed at mapping the geometry of the dark Universe. This mission, due for launch in 2020, will investigate the distance-redshift relationship and the evolution of cosmic structures by measuring shapes and redshifts of galaxies and clusters of galaxies out to redshifts ~ 2 . Euclid is optimized for two primary cosmological probes: i) weak gravitational lensing: a method to map the dark matter and measure dark energy by measuring the distortions of galaxy images by mass inhomogeneities along the line of sight; ii) baryonic acoustic oscillations: BAO are wiggle patterns imprinted in the clustering of galaxies which provide a standard ruler to measure dark energy and the expansion of the Universe. Euclid will have two instruments: an optical camera that will image in one optical broad band and a near infrared instrument that will observe in the YJH bands, in imaging and slitless spectroscopy. Euclid will preferentially target star forming galaxies from $z \sim 1-2$, hence it will detect all clusters up to the proto-cluster regime.

6.4.6. Large Synoptic Survey Telescope

The Large Synoptic Survey Telescope (LSST) is an 8 m telescope in Chile with a FOV of

9.6 deg² that will repeatedly scan the southern sky, accumulating 1000 pairs of 15 second exposures through ugrizy filters. First light is planned for 2022. LSST will yield the main 20000 deg² through a deep/wide/fast survey (depth $r \sim 24.5$). The main scientific goal of LSST is to probe the physics of DE via weak lensing, baryonic acoustic oscillations, SN Ia, and cluster counts. The combination of probes can yield the precision to distinguish between models of dark energy by simultaneously measuring mass growth (weak lensing + cluster counts) and curvature (BAO + SN), LSST will tell us whether the recent cosmic acceleration is due to dark energy or modified gravity.

6.4.7. eRosita

eRosita is the primary instrument on board the Russian Spectrum Roentgen Gamma (SRG) satellite that will be launched in 2016 (L2 orbit). This X-ray telescope consists of 7 identical Wolter I mirror modules, and each module contains 54 nested mirror shells. This is a novel detector system based on the XMM-Newton pn-CCD technology. eRosita will perform a first imaging all-sky survey in the medium energy X-ray range up to 10 keV with an improved spectral and angular resolution ($\sim 25''$) relative to ROSAT. The goal of eRosita is to detect the hot intracluster medium of 50-100 thousand clusters and groups and hot gas in filaments between clusters to map out the large scale structure in the Universe up to redshift ~ 1 , for the study of cosmic structure evolution.

Acknowledgements. I am grateful to the Scientific and Organizing Committees of the *Francesco Lucchin* school for the opportunity to deliver these lectures. It was a pleasure to listen to the other lecturers and I'm grateful to the participation of the students, who were engaged and inquisitive. I thank Paolo Tozzi for reviewing this contribution.

References

- Allen, S. W., Evrard, A. E., & Mantz, A. B. 2011, *ARA&A*, 49, 409
- Arnaud, K. A. 1996, in *Astronomical Data Analysis Software and Systems V*, G.H. Jacoby and J. Barnes eds. (ASP, San Francisco), ASP Conf. Ser., 101, 17
- Arnaud, M., Pratt, G. W., Piffaretti, R., et al. 2010, *A&A*, 517, A92
- Balestra, I., Tozzi, P., Ettori, S., et al. 2007, *A&A*, 462, 429
- Bañados, E., Venemans, B., Walter, F., et al. 2013, *ApJ*, 773, 178
- Bardeen, J. M., et al. 1986, *ApJ*, 304, 15
- Baum, W. A. 1959, *PASP*, 71, 106
- Bauer, F. E., et al. 2005, *MNRAS*, 359, 1481
- Bayliss, M. B., Ashby, M. L. N., Ruel, J., et al. 2014, *ApJ*, 794, 12
- Benson, B. A., de Haan, T., Dudley, J. P., et al. 2013, *ApJ*, 763, 147
- Bernardi, M. 2009, *MNRAS*, 395, 1491
- Böhringer, H., & Werner, N. 2010, *A&A Rev.*, 18, 127
- Borgani, S., Finoguenov, A., Kay, S. T., et al. 2005, *MNRAS*, 361, 233
- Brodwin, M., Brown, M. J. I., Ashby, M. L. N., et al. 2006, *ApJ*, 651, 791
- Calzetti, D. 2013, in *Secular Evolution of Galaxies*, J. Falcón-Barroso, J. H. Knapen eds. (Cambridge Univ. Press, new York), 419
- Cavagnolo, K. W., Donahue, M., Voit, G. M., & Sun, M. 2009, *ApJS*, 182, 12
- Cavaliere, A., & Fusco-Femiano, R. 1976, *A&A*, 49, 137
- Chen, Y., et al. 2007, *A&A*, 466, 805
- Coles, P., & Lucchin, F. 1995, *Cosmology: the origin and evolution of cosmic structure* (Wiley, Chichester)
- Chabrier, G. 2003, *PASP*, 115, 763
- Daddi, E., Dickinson, M., Morrison, G., et al. 2007, *ApJ*, 670, 156
- Daddi, E., et al. 2010, *ApJ*, 714, L118
- De Grandi, S., & Molendi, S. 2001, *ApJ*, 551, 153
- De Grandi, S., et al. 2004, *A&A*, 419, 7
- De Grandi, S., Santos, J. S., Nonino, M., et al. 2014, *A&A*, 567, A102
- De Lucia, G., & Blaizot, J. 2007, *MNRAS*, 375, 2
- Dole, H. A. 2015, *IAU General Assembly*, 21, 82963
- Dressler, A. 1980, *ApJ*, 236, 351
- Dunn, R.J.H., & Fabian, A.C., 2008, *MNRAS*, 385, 757
- Ebeling, H., & Wiedenmann, G. 1993, *Phys. Rev. E*, 47, 704
- Elbaz, D., Daddi, E., Le Borgne, D., et al. 2007, *A&A*, 468, 33
- Elbaz, D., Hwang, H. S., Magnelli, B., et al. 2010, *A&A*, 518, L29
- Elbaz, D., Dickinson, M., Hwang, H. S., et al. 2011, *A&A*, 533, A119
- Fabian, A.C., et al., 1994, *MNRAS*, 267, 779

- Fabian, A. C., Sanders, J. S., Allen, S. W., et al. 2011, *MNRAS*, 418, 2154
- Fassbender, R., Nastasi, A., Santos, J. S., et al. 2014, *A&A*, 568, A5
- Feretti, L., et al. 2012, *A&A Rev.*, 20, 54
- Fisher, D. B., & Drory, N. 2008, *AJ*, 136, 773
- Genzel, R., Tacconi, L. J., Gracia-Carpio, J., et al. 2010, *MNRAS*, 407, 2091
- Giodini, S., Lovisari, L., Pointecouteau, E., et al. 2013, *Space Sci. Rev.*, 177, 247
- Gladders, M. D., & Yee, H. K. C. 2000, *AJ*, 120, 2148
- Gobat, R., Rosati, P., Strazzullo, V., et al. 2008, *A&A*, 488, 853
- Gobat, R., Daddi, E., Onodera, M., et al. 2011, *A&A*, 526, A133
- Gobat, R., Strazzullo, V., Daddi, E., et al. 2013, *ApJ*, 776, 9
- Hasselfield, M., Hilton, M., Marriage, T. A., et al. 2013, *JCAP*, 7, 008
- Hudson, D. S., Mittal, R., Reiprich, T. H., et al. 2010, *A&A*, 513, A37
- Huertas-Company, M., Mei, S., Shankar, F., et al. 2013, *MNRAS*, 428, 1715
- Kaiser, N. 1986, *MNRAS*, 222, 323
- Kennicutt, R. C., & Evans, N. J. 2012, *ARA&A*, 50, 531
- Kroupa, P. 2001, *MNRAS*, 322, 231
- Lidman, C., Suherli, J., Muzzin, A., et al. 2012, *MNRAS*, 427, 550
- Liu, T., Tozzi, P., Tundo, E., et al. 2015, *ApJS*, 216, 28
- Madau, P., Ferguson, H. C., Dickinson, M. E., et al. 1996, *MNRAS*, 283, 1388
- Markevitch, M., Sarazin, C. L., & Vikhlinin, A. 1999, *ApJ*, 521, 526
- McDonald, M., Bayliss, M., Benson, B. A., et al. 2012, *Nature*, 488, 349
- McDonald, M., McNamara, B. R., van Weeren, R. J., et al. 2015, *ApJ*, 811, 111
- McNamara, B. R., & Nulsen, P. E. J. 2007, *ARA&A*, 45, 117
- Mei, S., Holden, B. P., Blakeslee, J. P., et al. 2009, *ApJ*, 690, 42
- Mewe, R., Gronenschild, E. H. B. M., & van den Oord, G. H. J. 1985, *A&AS*, 62, 197
- Milkeraitis, M., van Waerbeke, L., Heymans, C., et al. 2010, *MNRAS*, 406, 673
- Miley, G. K., Overzier, R. A., Zirm, A. W., et al. 2006, *ApJ*, 650, L29
- Miley, G., & De Breuck, C. 2008, *A&A Rev.*, 15, 67
- Million, E. T., & Allen, S. W. 2009, *MNRAS*, 399, 1307
- Mullis, C. R., Rosati, P., Lamer, G., et al. 2005, *ApJ*, 623, L85
- Papovich, C., Momcheva, I., Willmer, C. N. A., et al. 2010, *ApJ*, 716, 1503
- Peacock, J. A. 1999, *Cosmological Physics* (Cambridge Univ. Press, Cambridge)
- Peebles, P. J. E. 1993, *Principles of Physical Cosmology* (Princeton Univ. Press, Princeton)
- Peres, C.B., et al. 1998, *MNRAS*, 298, 416
- Peterson, J. R., & Fabian, A. C. 2006, *Phys. Rep.*, 427, 1
- Pilbratt, G. L., Riedinger, J. R., Passvogel, T., et al. 2010, *A&A*, 518, L1
- Planck Collaboration, Ade, P. A. R., Aghanim, N., et al. 2015, *arXiv:1502.01598*
- Poggianti, B. M., Aragón-Salamanca, A., Zaritsky, D., et al. 2009, *ApJ*, 693, 112
- Popesso, P., Biviano, A., Finoguenov, A., et al. 2015, *A&A*, 579, A132
- Postman, M., Lubin, L. M., Gunn, J. E., et al. 1996, *AJ*, 111, 615
- Press, W. H., & Schechter, P. 1974, *ApJ*, 187, 425
- Rodighiero, G., Daddi, E., Baronchelli, I., et al. 2011, *ApJ*, 739, L40
- Rosati, P., et al. 1995, *ApJ*, 445, L11
- Rosati, P., Borgani, S., & Norman, C. 2002, *ARA&A*, 40, 539
- Rosati, P., Tozzi, P., Gobat, R., et al. 2009, *A&A*, 508, 583
- Rozo, E., Vikhlinin, A., & More, S. 2012, *ApJ*, 760, 67
- Rykoff, E. S., et al. 1955, *ApJ*, 121, 161
- Salpeter, E. E. 1955, *ApJ*, 121, 161
- Santos, J.S., et al. 2008, *A&A*, 483, 35
- Santos, J.S., et al. 2010, *A&A*, 521, A64
- Santos, J. S., Fassbender, R., Nastasi, A., et al. 2011, *A&A*, 531, L15
- Santos, J. S., et al. 2012, *A&A*, 539, A105
- Santos, J. S., Altieri, B., Valtchanov, I., et al. 2015, *MNRAS*, 447, L65
- Sersic, J. L. 1968, *Atlas de galaxias australes* (Observatorio Astronomico, Cordoba, Argentina)
- Shankar, F., Marulli, F., Bernardi, M., et al. 2013, *MNRAS*, 428, 109
- Smith, R. K., et al. 2001, *ApJ*, 556, L91
- Strateva, I., Ivezić, Ž., Knapp, G. R., et al. 2001, *AJ*, 122, 1861
- Strazzullo, V., Rosati, P., Pannella, M., et al. 2010, *A&A*, 524, A17
- Tanaka, M., Finoguenov, A., & Ueda, Y. 2010, *ApJ*, 716, L152
- Thomas, D., et al. 2005, *ApJ*, 621, 673
- Tozzi, P., & Norman, C. 2001, *ApJ*, 546, 63

- Tozzi, P., Santos, J. S., Jee, M. J., et al. 2015, ApJ, 799, 93
- Tran, K.-V. H., Papovich, C., Saintonge, A., et al. 2010, ApJ, 719, L126
- Treu, T., Ellis, R. S., Kneib, J.-P., et al. 2003, ApJ, 591, 53
- Umetsu, K. 2010, [arXiv:1002.3952](https://arxiv.org/abs/1002.3952)
- Valtchanov, I., Pierre, M., & Gastaud, R. 2001, A&A, 370, 689
- Venemans, B. P., Röttgering, H. J. A., Miley, G. K., et al. 2007, A&A, 461, 823
- Visvanathan, N., & Sandage, A. 1977, ApJ, 216, 214
- Voit, G. M. 2005, Reviews of Modern Physics, 77, 207
- von der Linden, A., et al. 2007, MNRAS, 379, 867
- Webb, T. M. A., O'Donnell, D., Yee, H. K. C., et al. 2013, AJ, 146, 84
- Weinmann, S. M., Kauffmann, G., van den Bosch, F. C., et al. 2009, MNRAS, 394, 1213